JCI insight

RESEARCH ARTICLE

Disease-modifying bioactivity of intravenous cardiosphere-derived cells and exosomes in *mdx* mice

Russell G. Rogers, Mario Fournier, Lizbeth Sanchez, Ahmed G. Ibrahim, Mark A. Aminzadeh, Michael I. Lewis, and Eduardo Marbán

Smidt Heart Institute, Cedars-Sinai Medical Center, Los Angeles, California, USA.

Dystrophin deficiency leads to progressive muscle degeneration in Duchenne muscular dystrophy (DMD) patients. No known cure exists, and standard care relies on the use of antiinflammatory steroids, which are associated with side effects that complicate long-term use. Here, we report that a single intravenous dose of clinical-stage cardiac stromal cells, called cardiosphere-derived cells (CDCs), improves the dystrophic phenotype in *mdx* mice. CDCs augment cardiac and skeletal muscle function, partially reverse established heart damage, and boost the regenerative capacity of skeletal muscle. We further demonstrate that CDCs work by secreting exosomes, which normalize gene expression at the transcriptome level, and alter cell signaling and biological processes in *mdx* hearts and skeletal muscle. The work reported here motivated the ongoing HOPE-2 clinical trial of systemic CDC delivery to DMD patients, and identifies exosomes as next-generation cell-free therapeutic candidates for DMD.

Introduction

Duchenne muscular dystrophy (DMD) is a heritable myodegenerative disease affecting 1 in approximately 5,000 live-born males in the United States. Genetic lesions at the *Dmd* gene locus cause incomplete or incorrect translation of the full-length transcript, leading to virtual absence of functional dystrophin (1). This protein connects the intracellular cytoskeleton to the extracellular matrix, providing dynamic shock absorption and membrane stability during muscle contraction. Absence of dystrophin in striated muscle leads to membrane fragility, muscle damage, and disrupted cell signaling, which engender inflammation, fibrosis, and ultimately degeneration. In DMD patients, these pathophysiological processes manifest early as muscle weakness, and later as loss of ambulation and premature death due to respiratory or heart failure (2).

There is currently no cure for DMD, and the most commonly prescribed drugs are corticosteroids, which have not been shown to decrease the incidence of DMD-related cardiomyopathy. In fact, DMD patients treated with corticosteroids earlier, rather than later, have a higher risk of developing respiratory dysfunction and heart disease (3). Cardiosphere-derived cells (CDCs) are cardiac progenitor/stromal cells with antiinflammatory, antioxidant, antifibrotic, and cardiomyogenic properties (4). Given the apt match between the therapeutic actions of CDCs and the pathophysiology underlying DMD, CDCs represent a logical therapeutic candidate. We have recently shown that injecting CDCs directly into the myocardium of *mdx* mice resulted in profound phenotypic improvements in heart and skeletal muscle (5) — findings that motivated the HOPE-Duchenne clinical trial (ClinicalTrials.gov Identifier: NCT02485938).

The protean effects of CDCs appear to be mediated by the secretion of nanoparticles called exosomes (EXOs), which transfer genetic material to recipient cells to modify biological function (6, 7). Indeed, EXOs secreted by CDCs recapitulate the therapeutic benefits of CDCs when injected directly into the left ventricular myocardium of *mdx* mice (5). Because of the invasive nature of the delivery methods used in our previous work, we sought to determine if CDCs or EXOs would be bioactive when delivered intravenously — a clinically preferable method. Our earlier work reported in abstract form demonstrated that a single intravenous injection of CDCs or EXOs dramatically improved cardiac and skeletal muscle function in *mdx* mice (8, 9). We now report that CDCs and their EXOs, when delivered intravenously to aged *mdx* mice, boost cardiac and skeletal muscle function, partially reverse established heart damage, and amplify the regenerative capacity of skeletal muscle.

Conflict of interest: EM is a founding equity shareholder of Capricor Therapeutics and an unpaid member of its scientific advisory board.

Submitted: October 23, 2018
Accepted: February 14, 2019
Published: April 4, 2019.

Reference information: *JCI Insight*. 2019;4(7):e125754. https://doi.org/10.1172/jci.insight.125754.

Results

Intravenous CDC or EXO delivery promotes cardiorespiratory benefits. To test the effectiveness of an intravenous infusion of CDCs or EXOs, we first assessed baseline exercise capacity and in vivo cardiac function (see Figure 1A for experimental overview). Relative to wild-type (WT) mice, aged *mdx* mice display exercise intolerance (Figure 1B) and cardiac dysfunction (Figure 1D). Syngeneic CDCs were characterized by flow cytometry and determined to be $CD105^+$, $CD140b^+$, $Sca\text{-}1^+$, $CD31^-$, $CD45^-$, $CD90^-$, and $cKit^-$ (Supplemental Figure 1A; supplemental material available online with this article; https://doi.org/10.1172/jci.insight.125754DS1), consistent with previous reports (10). Human CDCs were serum starved and cultured in hypoxia for 24 hours prior to harvest of conditioned media and were characterized by nanoparticle tracking analysis and immunoblot (Supplemental Figure 1, B and C). A single intravenous dose of CDCs or EXOs (but not of vehicle alone) improved the maximal exercise capacity of *mdx* mice 3 weeks following treatment, and this improvement persisted for at least 6 weeks after CDC treatment (Figure 1, B and C). In parallel, CDC and EXO treatment both boosted cardiac ejection fraction relative to vehicle-treated *mdx* mice (Figure 1D), with an underlying reduction in myocardial fibrosis (Figure 1, E and F). It should be noted that due to the focal nature of fibrosis, Masson's trichrome staining may not completely reflect global changes in collagen deposition but may reflect alterations in the distribution of collagen within the heart. For WT controls (dashed lines, Figure 1, B and D, and WT in subsequent figures), we studied the nominal background strain of *mdx* mice (C57BL10/ScSn/J), rather than nonaffected littermates (of which there were none, given the homozygosity of the mutation in inbred *mdx* females). Regardless, the main focus here is on comparisons among *mdx* subgroups (injected with vehicle, CDC, or EXO).

To probe the mechanisms of benefit, we performed RNA sequencing (RNA-seq). In vehicle-treated *mdx* hearts, 772 genes were differentially expressed (DEGs) (Supplemental Figure 2A). Kyoto Encyclopedia of Genes and Genomes (KEGG) enrichment analysis grouped the DEGs into several pathways involved in inflammation such as cytokine-receptor interaction, complement and coagulation cascades, and TNF signaling (Supplemental Figure 2B). Importantly, transcriptome analysis of CDC- and EXO-treated *mdx* hearts revealed a reversal of the transcriptome, consistent with partial normalization of gene expression (Figure 2A). In addition, gene ontology (GO) enrichment analysis showed an overrepresentation of stem cell proliferation, somatic stem cell population maintenance, DNA demethylation, and DNA condensation and replication in CDC-treated *mdx* hearts (Supplemental Figure 2C). Moreover, GO enrichment analysis showed an overrepresentation of negative regulation of inflammatory response, positive regulation of cell cycle, and several processes involved in transcription in EXO-treated *mdx* hearts (Supplemental Figure 3). Based on these findings and known actions of CDCs (4, 11), we assessed the ability of CDCs and EXOs to alleviate inflammation and promote cardiomyogenesis.

Nuclear factor κB (NF-κB), a master regulator of inflammatory gene expression, was activated in vehicle-treated *mdx* hearts (Figure 2B). Phosphorylated NF-κB translocates to the nucleus and induces the transcription of several proinflammatory cytokines and chemokines. In vehicle-treated *mdx* hearts, activated NF-κB signaling was accompanied by an accumulation of $CD68^+$ macrophages (Figure 2, C and D). Both CDC and EXO treatment attenuated NF-κB phosphorylation and macrophage infiltration in *mdx* hearts (Figure 2, B–D). Because inflammation is often associated with oxidant stress (12), we probed for the formation of protein-carbonyl adducts — an irreversible oxidative modification in which damaged proteins must be degraded by the proteasome. Relative to WT hearts, vehicle-treated *mdx* hearts contained more protein-carbonyl adducts, which were reduced to WT levels by CDC and EXO treatment (Figure 2E).

To assess effects on cardiomyogenesis, we quantified proliferating ($Ki\text{-}67^+$) cardiomyocytes. Previous work demonstrates that small mononuclear cardiomyocytes reenter the cell cycle (expressing Ki-67) and contribute to cardiac repair following myocardial infarction (13). Vehicle-treated *mdx* hearts exhibit a basal level of $Ki\text{-}67^+$ cardiomyocytes, presumably as a compensation for ongoing cardiomyocyte loss (Figure 2, F and G). When *mdx* mice were treated with CDCs or EXOs, the number of proliferating cardiomyocytes nearly tripled. A *Z*-stacked video of $Ki\text{-}67^+$ cardiomyocyte nuclei, demonstrating vertical and horizontal overlay among Ki-67, DAPI, and α-sarcomeric actinin (Supplemental Video 1), verifies nuclear localization of Ki-67 within cardiomyocytes. Because *mdx* hearts and cardiomyocytes derived from human Duchenne induced pluripotent stem cells display striking mitochondrial dysfunction (11), we quantified the protein expression of subunits comprising complexes I–V of the electron transport chain (ETC). Relative to WT hearts, vehicle-treated *mdx* hearts exhibit lower protein levels of ETC complexes, which were restored by CDC and EXO treatment (Figure 2, H and I). Together, these data

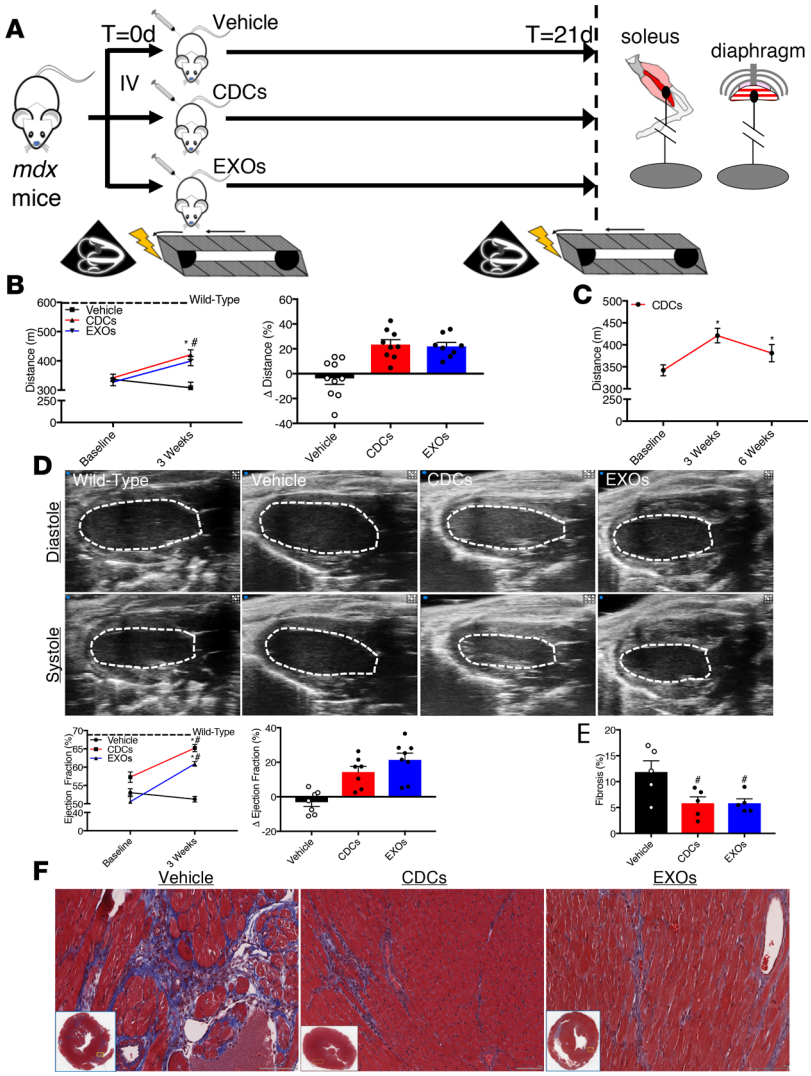

Figure 1. Cardiorespiratory benefits of systemic CDC or EXO delivery. (**A**) Schematic of the experimental design. Mice underwent baseline testing of exercise capacity and cardiac function, and then were injected with vehicle control (Dulbecco's PBS; 100 μl), cardiosphere-derived cells (CDCs; 2.5×10^5 cells per 100 μl), or CDC-derived exosomes (EXOs; 2.0×10^9 particles per 100 μl) into the femoral vein. Animals were reassessed for exercise capacity and cardiac function 3 weeks later. (**B** and **C**) Exercise capacity, as determined by a graded exercise test, was significantly improved in CDC- and EXO-treated *mdx* mice after 3 weeks (n = 8–10 per group; WT n = 9). This effect was maintained for at least 6 weeks following CDC treatment (n = 5). (**D**) Representative echocardiogram tracings. Cardiac function, as measured by transthoracic echocardiography, was significantly improved in CDC- and EXO-treated *mdx* mice after 3 weeks (n = 7–8 per group; WT n = 7). (**E**) Pooled data from **F** reveal less interstitial fibrosis in CDC- and EXO-treated *mdx* hearts (n = 5 per group). (**F**) Representative Masson's trichrome–stained micrographs from vehicle-treated, CDC-treated, and EXO-treated *mdx* hearts. Scale bars: 100 μm. Bar graphs depict mean ± SEM. Statistical significance was determined by ANOVA with $P \leq 0.05$. When appropriate, a Newman-Keuls correction for multiple comparisons was applied. *Significantly different from baseline; #significantly different from vehicle. Dashed line represents mean of WT values.

demonstrate that CDCs and EXOs partially reverse established heart damage by attenuating fibrosis, decreasing inflammation, enhancing cardiomyogenesis, and normalizing mitochondrial protein deficits.

Skeletal muscle improvements by intravenously delivered CDCs or EXOs. To determine if systemic delivery of CDCs or EXOs would also benefit skeletal muscles of *mdx* mice, we first examined the contractile properties of the soleus and diaphragm — major muscles involved in locomotion and respiration, respectively (see Figure 1A for an experimental overview). Relative to WT muscles, solei and diaphragms from vehicle-treated *mdx* mice produce less twitch and tetanic force (Figure 3, A–C and Supplemental Figure 4, A–C). CDC and EXO treatment significantly increased isometric force in *mdx*

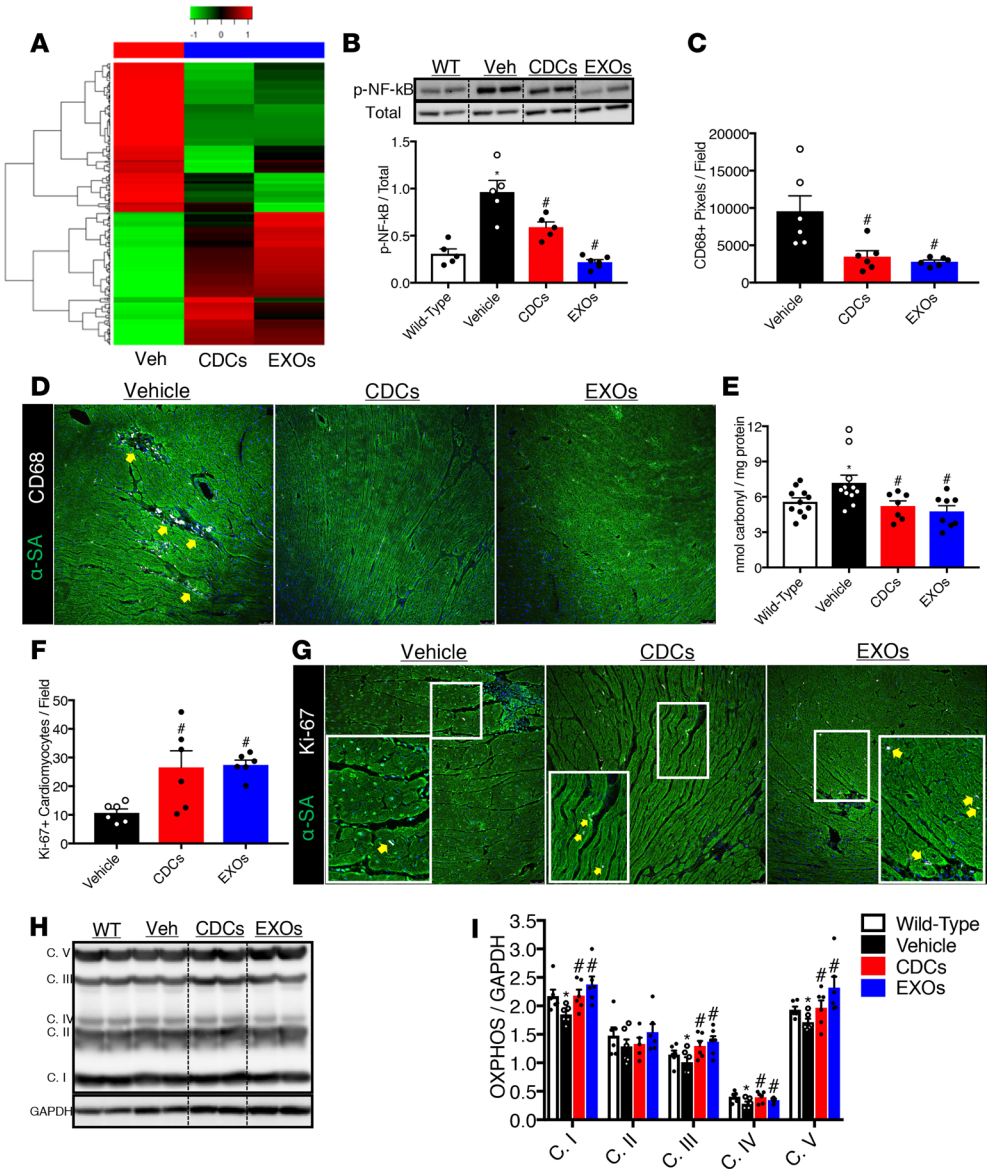

Figure 2. Biological effects of CDC or EXO treatment in *mdx* mouse hearts. (**A**) Transcriptome analysis of vehicle, cardiosphere-derived cell–treated (CDC-treated), and CDC-derived exosome–treated (EXO-treated) *mdx* hearts using 2-dimensional hierarchical clustering of genes with at least 1.5-fold change between WT/vehicle, CDC/vehicle, and EXO/vehicle. Both CDC and EXO treatment reversed the transcriptomic profile and partially normalized gene expression. (**B**) Representative NF-κB immunoblot and quantification of NF-κB phosphorylation in *mdx* hearts (n = 5 per group). Both CDC and EXO treatment reduced NF-κB phosphorylation. (**C**) Pooled data of $CD68^+$ pixels from **D** reveal that CDC and EXO treatment reduces macrophage abundance (n = 6 per group). (**D**) Immunohistochemical staining for CD68 and α-sarcomeric actinin (α-SA) in vehicle-, CDC-, and EXO-treated *mdx* hearts. Scale bars: 50 μm. (**E**) Colorimetric analysis of protein-carbonyl adducts reveal normalization by CDC and EXO treatment (n = 7–11 per group). (**F**) Pooled data of $Ki\text{-}67^+$ cardiomyocytes from **F** reveal that CDC and EXO treatment induces cardiomyocyte proliferation (n = 6 per group). (**G**) Immunohistochemical staining for Ki-67 and α-SA in vehicle-, CDC-, and EXO-treated *mdx* hearts. Scale bars: 50 μm. (**H**) Representative immunoblot of mitochondrial electron transport chain complex subunits. (**I**) Pooled data from **H** reveal that CDC and EXO treatment restores the protein levels of complexes involved in oxidative phosphorylation (OXPHOS) (n = 5–6 per group). Bar graphs depict mean ± SEM. Statistical significance was determined by ANOVA with $P \leq 0.05$. When appropriate, a Newman-Keuls correction for multiple comparisons was applied. *Significantly different from WT; #significantly different from vehicle. Dashed lines in **B** and **H** represent splice sites among lanes run on the same immunoblot.

solei (Figure 3, A–C) and trended favorably in the *mdx* diaphragm (Supplemental Figure 4, A–C). The increased developed force by *mdx* solei due to CDC or EXO treatment was associated with improved muscle architecture, reduced interstitial fibrosis, and a 2-fold increase in the number of myofibers (Figure 3, D–F).

KEGG enrichment analysis of the vehicle-treated *mdx* soleus grouped 2,186 DEGs into several categories including proinflammatory classifications such as cytokine-receptor interaction, chemokine signaling, and leukocyte transendothelial migration (Supplemental Figure 4, D and E). As in the *mdx* heart, CDC and EXO treatment reversed the transcriptomic profile in the *mdx* soleus (Figure 3G). Ingenuity Pathway Analysis (IPA) of pathways/networks altered due to CDC treatment revealed that 307 DEGs were related to "skeletal muscle function or disease," and of those, 171 genes were related to myogenesis (Supplemental Figure 4F). In parallel, GO enrichment analysis revealed an overrepresentation of positive regulation of immune response, angiogenesis, and stem cell proliferation (Supplemental Figure 4G). Based on these findings, which are consistent with those in *mdx* hearts, we examined the ability of CDCs and EXOs to modulate inflammation and skeletal myogenesis.

In vehicle-treated *mdx* solei, phosphorylated NF-κB (Figure 3H) was also associated with an accumulation of $CD68^+$ macrophages (Figure 3, I and J). CDC treatment increased both phosphorylated NF-κB and total NF-κB, as determined by immunoblot, which was associated with an accumulation of $CD68^+$ macrophages relative to vehicle treatment (Figure 3, I and J). Moreover, EXO treatment preserved NF-κB phosphorylation and was also associated with an accumulation of $CD68^+$ macrophages (Figure 3, I and J). It should be noted that macrophages in vehicle-treated *mdx* solei aggregate in necrotic lesions, while in CDC- and EXO-treated *mdx* solei macrophages become primarily oriented surrounding myofibers. This orientation has been observed during the wound-healing phase of skeletal muscle regeneration (14). Given that CDC- and EXO-treated *mdx* solei contain twice as many myofibers as vehicle-treated *mdx* solei, and RNA-seq indicates that CDC treatment promotes skeletal myogenesis, we assessed the effects of CDCs and EXOs on *mdx* muscle regeneration. Myogenesis begins with the activation of resident muscle stem cells (satellite cells), which proliferate and differentiate into myoblasts to form myotubes. Newly formed myotubes mature into adult myofibers, which are characterized by sequential expression of developmental and adult myosin heavy chain (MHC) isoforms. Neonatal MHC (nMHC) is a widely used marker for skeletal muscle regeneration. Relative to vehicle-treated *mdx* solei, CDC- and EXO-treated *mdx* solei contain twice as many $nMHC^+$ myofibers (Figure 3, K and L), consistent with IPA analysis indicating enrichment in pathways related to myogenesis. Together, these data support a role for CDCs and EXOs in the repair of dystrophic skeletal muscle.

Blockade of EXO biosynthesis renders CDCs nontherapeutic. Thus far, we have shown that EXOs mimic the effects of CDCs, but we have not shown that EXO secretion by CDCs is required. To test this idea, we used a small molecule (GW4869) to inhibit EXO biosynthesis in cultured CDCs (Supplemental Figure 5A). Exposure of CDCs to 20 μM GW4869 24 hours prior to injection into *mdx* mice undermined the benefits of CDCs. Unlike control CDCs, GW4869-exposed CDCs failed to improve exercise capacity above vehicle-treated levels (Supplemental Figure 5B). In parallel, the improvement in in vivo cardiac ejection fraction was blunted by GW4869 (Supplemental Figure 5C). Likewise, contractile force of the *mdx* diaphragm with CDC-GW4869 treatment was not different from treatment with vehicle only (Supplemental Figure 5, D–F). In contrast, there was a similar improvement in contractile force of the *mdx* solei with CDC and CDC-GW4869 treatment (Supplemental Figure 5, G–I). The basis of the differential effect of GW4869-treated CDCs on solei and diaphragm is unclear. Nevertheless, the majority of the data support the notion that CDCs primarily exert their therapeutic benefits via the secretion of EXOs.

Exosomal miR-148a augments myogenesis in mdx skeletal muscle. Under hypoxic culture conditions, CDCs secrete EXOs with a high abundance of the microRNA (miR) miR-148a, which partially mimics the effects of CDC EXOs (11). Likewise, quantitative PCR (qPCR) analysis confirmed that miR-148a is packaged into the EXOs used in this study with an 8-fold higher abundance than in the parent CDCs (Figure 4A). A previous study (15) reported that miR-148a promotes differentiation of myogenic precursor cells in vitro. To determine if exosomal transfer of miR-148a mediates (at least in part) the regenerative effects of EXOs in the *mdx* mouse soleus, we injected 200 ng of an antagomiR for miR-148a-3p (anti–miR-148a; Sigma-Aldrich) into the mouse soleus and a scrambled RNA control (Sigma-Aldrich) into the contralateral muscle, and then treated the mice with EXOs (see Figure 4B for an experimental overview). Forty-eight hours after injections, anti–miR-148a decreased miR-148a expression in the EXO-treated *mdx* soleus 5-fold (Figure 4C). Three weeks after injections, *mdx* solei injected with anti–miR-148a contained significantly fewer myofibers than the contralateral muscle injected with scramble (Figure 4, D and E). This effect was paralleled by a significant decrease in the number of $nMHC^+$

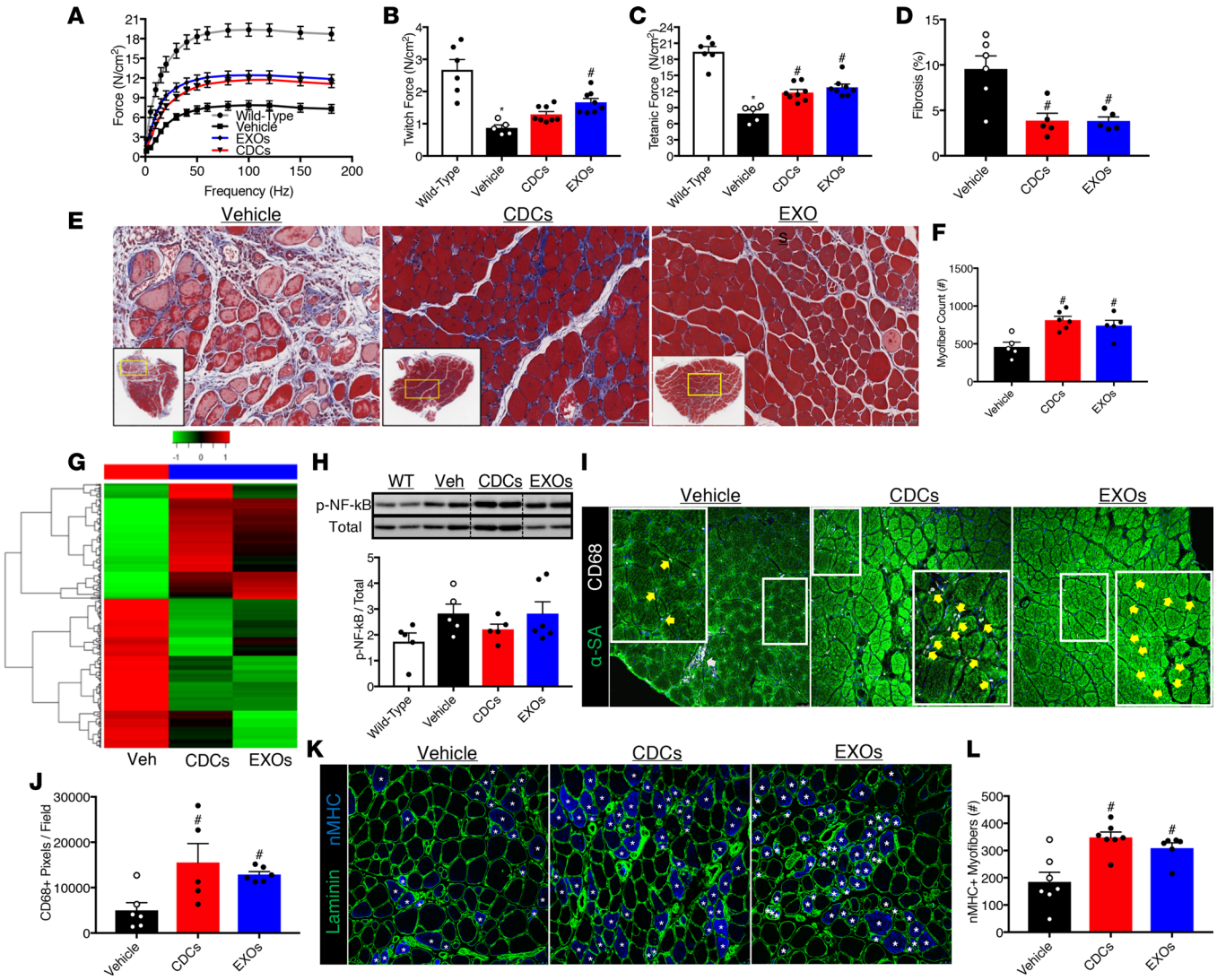

Figure 3. Skeletal muscle improvements by systemic CDC or EXO delivery. (**A**) In vitro force-frequency relationship of WT, vehicle-, cardiosphere-derived cell–treated (CDC-treated), or CDC-derived exosome–treated (EXO-treated) *mdx* solei (n = 5–8 per group). Both CDC and EXO treatment shifted the force-frequency curve up and to the left. (**B**) Twitch and (**C**) tetanic force derived from **A** demonstrate that CDC and EXO treatment boosts the developed force by *mdx* solei (n = 5–8 per group). (**D**) Pooled data from **E** reveal less interstitial fibrosis in CDC- and EXO-treated *mdx* solei (n = 5–6 per group). (**E**) Representative Masson's trichrome–stained micrographs from vehicle-, CDC-, and EXO-treated *mdx* solei. Scale bars: 100 μm. (**F**) Pooled data from **E** reveal more total myofibers in CDC- and EXO-treated *mdx* solei (n = 5–6 per group). (**G**) Transcriptome analysis of vehicle-, CDC-, and EXO-treated *mdx* solei using 2-dimensional hierarchical clustering of genes with at least 1.5-fold change between vehicle/WT, CDC/vehicle, and EXO/vehicle. Both CDC and EXO treatment reversed the transcriptomic profile and partially normalized gene expression. (**H**) Representative NF-κB immunoblot and quantification of NF-κB phosphorylation in *mdx* solei. CDC treatment normalized NF-κB phosphorylation (n = 5 per group). In contrast, NF-κB phosphorylation was preserved by EXO treatment (n = 5 per group). (**I**) Immunohistochemical staining for CD68 and α-sarcomeric actinin (α-SA) in vehicle-, CDC-, EXO-treated *mdx* solei. Scale bars: 50 μm. (**J**) Pooled data from **I** reveal a greater abundance of CD68$^+$ pixels in CDC- and EXO-treated *mdx* solei (n = 6–7 per group). (**K**) Immunohistochemical staining for neonatal myosin heavy chain (nMHC) and laminin in vehicle-, CDC-, and EXO-treated *mdx* solei. Scale bars: 50 μm. (**L**) Pooled data from **K** reveal more nMHC$^+$ myofibers in CDC- and EXO-treated *mdx* solei (n = 7 per group). Bar graphs depict mean ± SEM. Statistical significance was determined by ANOVA with $P \leq 0.05$. When appropriate, a Newman-Keuls correction for multiple comparisons was applied. *Significantly different from WT; #significantly different from vehicle. Dashed lines in **H** represent splice sites among lanes run on the same immunoblot.

myofibers in the anti–miR-148a–injected soleus (Figure 4, F and G). Toxicity of the RNA transfection reagent, as evidenced by histopathology reminiscent of chemically induced muscle injury (16), likely explains the decreased total number of myofibers and nMHC$^+$ myofibers when compared with muscles from EXO-treated *mdx* mice. Together, these data indicate that miR-148a delivered to skeletal muscles via CDC-derived EXOs participates in skeletal muscle regeneration in vivo.

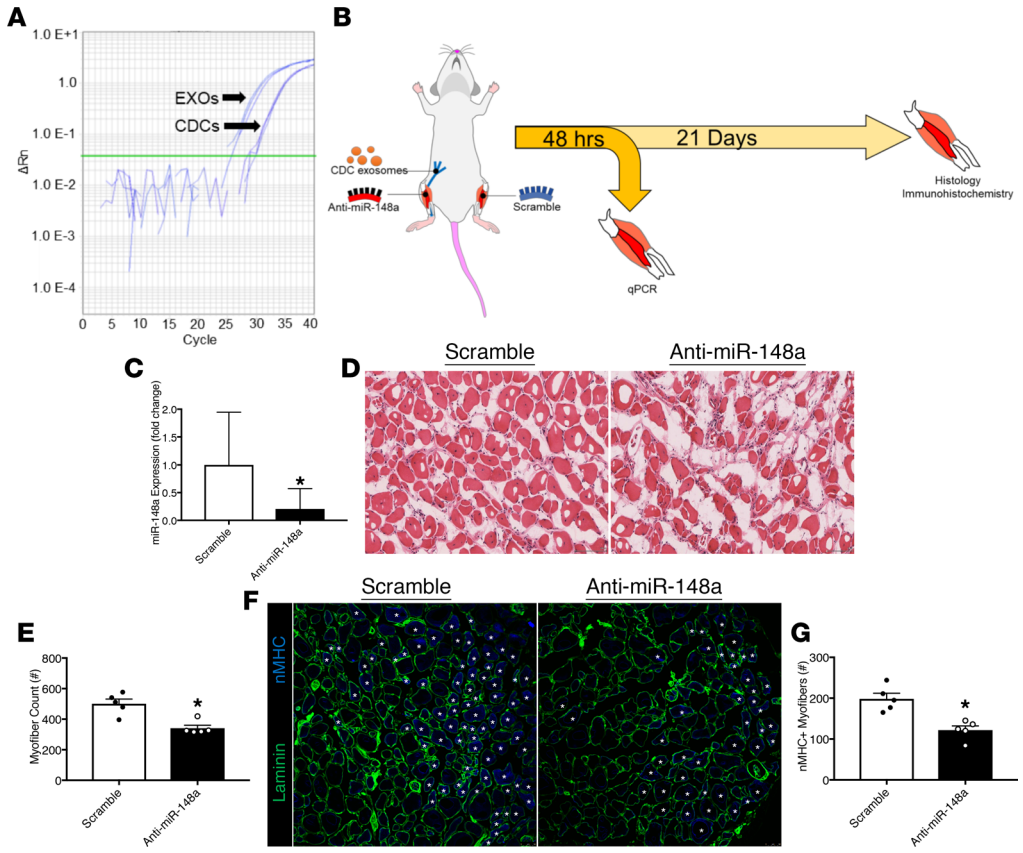

Figure 4. Exosomal miR-148a promotes *mdx* skeletal muscle regeneration. (**A**) Amplification plot from a qPCR analysis of miR-148a in human cardiosphere-derived cells (CDCs) and their exosomes (EXOs). EXOs contain an 8-fold higher abundance of miR-148a than their parent CDCs. (**B**) Schematic of the experimental design. (**C**) qPCR analysis of miR-148a expression in *mdx* solei 48 hours after injection of RNA scramble or anti–miR-148a. Anti–miR-148a–injected solei contained 5-fold less miR-148a than RNA scramble–injected solei. Fold change was calculated using the $2^{-\Delta\Delta Ct}$ method. Error bar reflects SEM of pooled ΔCt data (n = 3). (**D**) Representative hematoxylin and eosin–stained micrographs from RNA scramble control– and anti–miR-148a–injected *mdx* solei after 3 weeks. Scale bars: 100 μm. (**E**) Pooled data from **D** reveal more total myofibers in the RNA scramble–injected solei than in the anti–miR-148a–injected solei (n = 5). (**F**) Immunohistochemical staining for neonatal myosin heavy chain (nMHC) and laminin in RNA scramble control–injected and anti–miR-148a–injected *mdx* solei after 3 weeks. Scale bars: 50 μm. (**G**) Pooled data from **E** reveal more nMHC$^+$ myofibers in RNA scramble–injected solei than in the anti–miR-148a–injected solei (n = 5 per group). Bar graphs depict mean ± SEM. Statistical significance was determined by independent t tests with $P \leq 0.05$. *Significantly different from RNA scramble control.

Discussion

CDCs have been shown to promote tissue repair in several preclinical studies, including a DMD mouse model (11, 13, 17–20). Much of the previous work has focused on studying the therapeutic benefits associated with direct myocardial delivery. Here, we show that CDCs are efficacious at treating the heart and skeletal muscles of *mdx* mice when delivered intravenously — a clinically innocuous method. Consistent with previous reports, data presented here support the idea that CDCs work by secreting EXOs to antagonize multiple pathological processes active in DMD. Indeed, blocking EXO biosynthesis with GW4869 diminished the efficacy of CDCs, while treatment with EXOs purified from human CDCs mimicked the therapeutic benefits of CDCs. Transfer of exosomal contents such as RNA to recipient cells is sufficient to modify cell behavior (21–23). miRs are small noncoding RNAs highly enriched in EXOs and are known to regulate cellular gene expression. RNA-seq demonstrated that CDCs and their EXOs reversed the transcriptomic profile, and altered cell signaling and biological processes in *mdx* mouse hearts and skeletal muscles. We determined that miR-148a, a miR enriched in EXOs from hypoxic CDCs, is involved in *mdx* skeletal muscle regeneration. While we cannot exclude the possibility that other miRs or noncoding RNAs contained within EXOs may contribute to myogenesis, miR-148a is required, alone or in combination with other noncoding RNAs present in EXOs, to promote myogenesis.

In contrast to the *mdx* heart, we unexpectedly found that CDCs and their EXOs promote the accumulation of macrophages in *mdx* skeletal muscle 3 weeks following treatment. Based on data presented in Figure 3, we conclude that this observation is not pathological. Several lines of evidence support a positive role for macrophages in skeletal myogenesis: (a) depletion of macrophages impairs recovery from acute muscle injury (24), (b) satellite cells attract macrophages to enhance muscle growth (25), (c) macrophages modify myoblast proliferation and differentiation kinetics (26), and (d) macrophage polarization controls muscle stem cell fate and coordinates repair (27). Normally, macrophage infiltration in acutely injured muscle is resolved once repair has been completed. However, in *mdx* skeletal muscle, macrophages persistently accumulate and contribute to disease pathology (28). Increased macrophage infiltration, either in response to CDCs or their EXOs, is associated with reduced muscle pathology, suggesting that these macrophages support myogenesis rather than contribute to the disease. We have reported that macrophage depletion impairs recovery from downhill running in *mdx* mice (29), which suggests that a population of *mdx* macrophages are necessary for repair. EXOs derived from CDCs skew macrophage polarization to enhance efferocytosis and promote cardioprotection in acute myocardial infarction (21). Further, immunomodulation of macrophages by injection of a hydrogel scaffold containing a myostatin inhibitor into *mdx* skeletal muscle promotes tissue regeneration (30). These findings beg the investigation of exosomally triggered immunomodulation to promote *mdx* skeletal muscle regeneration; however, such experiments are beyond the scope of this report.

Given the preclinical insights reported here, CDCs are now being administered systemically in a placebo-controlled trial in DMD patients (HOPE-2; ClinicalTrials.gov Identifier: NCT03406780), thereby avoiding the need for cardiac catheterization as performed in the previous HOPE-Duchenne trial (31). In addition to CDCs themselves, EXOs derived from CDCs are a promising next-generation therapeutic candidate. We previously demonstrated that EXOs induce a transient reexpression of the full-length dystrophin protein when injected directly into the left ventricular cavity (11). Here, we show that 3 weeks after intravenous delivery, expression of the full-length dystrophin isoform is less than 0.5% of WT levels in the diaphragm and soleus of *mdx* mice (Supplemental Figure 6, A and B). Therefore, the therapeutic benefits reported here cannot be explained by rescue of dystrophin expression. Nevertheless, CDC-derived EXOs contain the necessary genetic material to reprogram recipient cells and alter their cellular function to achieve homeostasis in *mdx* hearts and skeletal muscles. The finding that human EXOs are therapeutic in *mdx* mice suggests such EXOs may be well tolerated in humans, and clinical-grade manufacturing is feasible (32). A single dose of either therapeutic candidate (CDCs or EXOs) is sufficient to partially reverse established muscle pathology, but repeated delivery may lead to greater improvements than those reported here. However, we have not yet empirically tested this conjecture.

Methods

Animals and injections. Ten- to 12-month-old female *mdx* (C57BL10/ScSn-DMD^{mdx}/J) and WT age- and strain-matched (C57BL10/ScSn/J) animals were used in this study. Mice were housed under pathogen-free conditions in a temperature-controlled room with a 12-hour photoperiod. Baseline measurements of maximal exercise capacity and in vivo cardiac function were recorded prior to injection. CDCs (2.5×10^5) and EXOs (2.0×10^9) were suspended in 100 μl of Dulbecco's PBS (DPBS) and injected into the femoral vein of *mdx* mice. Vehicle-treated *mdx* mice received an equal volume of DPBS injected into the femoral vein. Mice were reassessed for maximal exercise capacity and in vivo cardiac function 3 weeks after injection, and then tissues were harvested and processed for muscle physiology experiments, histology, and immunohistochemistry, or frozen in liquid nitrogen and stored at –80°C.

CDC culture and EXO purification. Mouse CDCs were generated from an 8-week-old strain-matched WT donor. The ventricles were cut into fragments <1 mm^3, washed, and partially digested with 0.05% trypsin (Gibco). These fragments were individually seeded onto fibronectin-coated culture dishes (Corning) and cultured in growth media (Iscove's Modified Dulbecco's Medium [GIBCO], 20% FBS [Atlas Biologicals], 1% penicillin/streptomycin [GIBCO], and 1× 2-mercaptoethanol [GIBCO]). After a variable period of growth, a monolayer of fibroblast-like adherent and phase-bright cells emerged from the explants. Both populations of cells surrounding the explants (termed explant-derived cells) were harvested using enzymatic digestion (TrypLE; GIBCO) and cultured in ultra-low adherent flasks (Corning) for 3 days. In suspension culture, explant-derived cells spontaneously form 3-dimensional clusters termed cardiospheres, which were harvested and plated in fibronectin-coated culture flasks. In adherent culture, cardiospheres form a monolayer of cells (CDCs). CDCs were expanded to passage 3–5, which

were used for all experiments. To block EXO biosynthesis, confluent CDCs were washed with DPBS and the media were supplanted with serum-free media. Twenty micromolar GW4869 (Sigma-Aldrich), a neutral sphingomyelinase inhibitor, was added to the media and the CDCs were cultured for an additional 24 hours. CDCs to be used for in vivo experiments were washed, enzymatically dissociated from the adherent culture dishes, washed again, counted, and suspended in DPBS. To generate EXOs, human CDCs were cultured until confluence at passage 5. The cells were washed with DPBS, and the media were supplanted with serum-free media. CDCs were then cultured at physiologically low oxygen (2% O_2) for 24 hours. The conditioned media were then collected, sterile filtered using a 0.45-μm filter, and the EXOs were purified and concentrated by ultrafiltration via centrifugation using 3-kDa MWCO centrifugal filters (EMD Millipore). EXO concentration (particles per ml) of the filtrate was measured by dynamic light scattering and nanoparticle tracking analysis (NanoSight NS300). EXOs were then aliquoted in ready-to-use tubes, frozen, and stored at –80°C until later use.

Flow cytometry. Cytometric analysis was performed to characterize the phenotype of mouse CDCs. Cells were harvested from culture at passage 5 and 1×10^6 CDCs were suspended in FACS buffer (5 ml FBS and 375 mg EDTA in 495 ml PBS). Cells were incubated with APC-, PE-, or FITC-conjugated antibodies against CD31, CD34, CD45, CD90, CD105, CD117 (c-Kit), Ly-6A/E (Sca-1), and CD140b antigens at a dilution of 1:100 for 1 hour at room temperature. Isotype-matched antibodies served as negative controls. Flow cytometry experiments were formed using a FACSCanto II flow cytometer (BD). Gates were established by forward and side scatter to exclude cellular debris. Fluorescence compensation was performed using single-labeled controls. Quantitative analysis was performed using FlowJo software (FlowJo LLC, v10). All antibodies were purchased from BD Bioscience except CD140b, which was purchased from BioLegend. Isotype antibodies were purchased from the respective vendor.

Treadmill exercise testing. Mice were placed inside an Exer-3/6 rodent treadmill (Columbus Instruments) equipped with a shock grid elevated 5 degrees. During the acclimatization period, mice were undisturbed for 30 minutes prior to engagement of the belt. After the belt engaged, mice were encouraged to familiarize themselves with walking on the treadmill at a pace of 10 m/min for an additional 20 minutes. After the acclimatization period, the exercise protocol engaged (shock grid activated at 0.15 mA with a frequency of 1 shock/s). This protocol is intended to induce volitional exhaustion by accelerating the belt speed by 1 m/min per minute. Mice that rest on the shock grid for more than 10 seconds with nudging were considered to have reached their maximal exercise capacity (their accumulated distance traveled is recorded) and the exercise test was terminated.

Echocardiography. Mice underwent 2-dimensional transthoracic echocardiography at baseline (prior to treatment) and 3 weeks after treatment. After the induction of light isoflurane anesthesia, parasternal long-axis B-mode videos were recorded (Vevo 3100, Visual Sonics) and left ventricular ejection fraction was measured with Visual Sonics v2.0.0 software. Measurements were obtained on 3 or more consecutive cardiac cycles and averaged for each mouse.

In vitro–isolated skeletal muscle physiology. Whole-muscle physiology was performed as described previously (33), with slight modifications. Briefly, mice were deeply anesthetized with isoflurane inhalation and the soleus or diaphragm muscles were rapidly excised. Following a lateral midline skin incision of the lower leg the soleus was dissected and isolated and its tendons of origin and insertion were tightened with 3-0 silk suture and rapidly excised. The soleus muscle was vertically mounted in a tissue bath containing a mammalian Ringer's of the following composition: (in mM) 137 NaCl, 5 KCl, 2 $CaCl_2$, 1 $MgSO_4$, 1 NaH_2PO_4, 24 $NaHCO_3$, 11 glucose. The solution was constantly aerated with 95% O_2 and 5% CO_2 with pH maintained at 7.35 and temperature kept at 24°C. Following a left costal margin skin and muscle incision, a section of the midcostal hemidiaphragm was transferred to a preparatory Sylgar-lined dish containing the aerated cold Ringer's and a narrow 3- to 4-mm-wide strip of diaphragm was isolated, maintaining fiber attachments to the rib and central tendon intact, which were tightened with silk suture and mounted vertically in the tissue bath. One end of the soleus or diaphragm was secured to a clamp at the bottom of the dish and one was attached to a calibrated force transducer (Model 300B, Cambridge Technology). A micromanipulator linked to the system was used to adjust muscle length. Platinum wire electrodes placed on each side of the muscle were used for direct muscle stimulation (Grass Model S88 Stimulator) using 0.2-ms-duration monophasic rectangular pulses of constant current (Mayo Engineering) delivered at supramaximal intensity. Muscle preload was incrementally adjusted until the optimal muscle length for maximum isometric twitch force (Lo) was reached. Lo was measured at 0.1-mm accuracy using a digital caliper. Isometric contractile properties were then determined at this Lo. Peak twitch force was determined from a single pulse. Force-frequency

relationships were measured at stimulus frequencies ranging from 5 to 180 pulses per second. The stimuli were presented in trains of 1-s duration with an interval of at least 1 minute intervening between each stimulus train. Muscle forces generated, including twitch and maximum tetanic force, were normalized for the estimated physiological cross-sectional area (CSA) of the muscle segment (CSA = muscle weight/1.056 × Lo; where 1.056 g/cm^3 represents the density of muscle) and expressed in Newtons (N)/cm^2. For the soleus muscle, Lo was also normalized for muscle fiber length (0.71 of Lo) in estimating muscle specific force.

RNA purification, qPCR analysis, and RNA-seq. Total RNA, including small RNAs of approximately 18 nucleotides and greater were purified using the miRNeasy Mini Kit (Qiagen) according to the manufacturer's recommended protocol. For qPCR, cDNA was synthesized using the QuantiMir RT Kit (System Biosciences) per the manufacturer's protocol. PCR products were analyzed using Applied Biosystems 7900HT PCR system. Five hundred nanograms of cDNA was amplified using SYBR Green PCR master mix (Qiagen). The forward primer for miR-148a was the mature miR-148a-3p sequence (5′-UCAGUGCACUACAGAACUUUGU-3′). A forward primer for miR-16 (5′-UAGCAGCACGUAAAUAUUGGCG-3′) was provided by the QuantiMir kit and used as an endogenous reference control. A universal reverse primer was provided by the kit. Cycling conditions were performed according to the QuantiMir kit protocol. Where appropriate, the $2^{-\Delta\Delta Ct}$ method was used to determine gene expression fold change. For RNA-seq, a sequencing library was constructed using the TruSeq Stranded Total RNA with Ribo-Zero kit (Illumina) per the manufacturer's recommended protocol. Sequencing was performed using a HiSeq 4000 (Illumina) sequencing system. All RNA-seq data were deposited in the NCBI's Gene Expression Omnibus database (GEO GSE124068). Reads were mapped to the latest UCSC transcript set using Bowtie2 v2.1.0 and gene expression level was estimated using RSEM v1.2.15. Trimmed mean of M-values was used to normalize gene expression. DEGs were identified using edgeR software. Genes with greater than 1.5-fold change and $P < 0.05$ were considered differentially expressed. Pathway and network analyses were performed using IPA software (Qiagen). The canonical pathways generated by IPA are the most significant for the data sets. Fischer's exact test with a false discovery rate option was used to calculate the significance of each pathway.

Immunoblot. Ice-cold RIPA lysis buffer (Thermo Fisher Scientific) supplemented with a protease/phosphatase inhibitor cocktail and EDTA (Thermo Fisher Scientific) was added to the heart and soleus that were then homogenized using an electric homogenizer and processed for immunoblotting as previously described (34). Briefly, the homogenate was then centrifuged at 14,000 *g* for 30 minutes at 4°C and the pellet was discarded. Total protein concentration of the supernatant was measured using a bicinchoninic acid (BCA) assay (Thermo Fisher Scientific). Tissue homogenates were diluted using 4× LDS sample buffer, 10× reducing agent, and normalized by volume with RIPA lysis buffer. Thirty micrograms of protein was resolved in a 4%–12% Bis-Tris sodium dodecyl sulfate (SDS) polyacrylamide gel (Novex) at 130 V for 60 minutes (2.5 hours for dystrophin). Proteins were then immobilized on a PVDF (Thermo Fisher Scientific) membrane using a wet transfer module (Bio-Rad) at 300 mA for 1.5 hours (3.0 hours for dystrophin). Membranes were then blocked for 1 hour at room temperature in 5% (w/v) nonfat dried milk (Bio-Rad) dissolved in Tris-buffered saline with 0.05% Tween 20 (TBS-T; Thermo Fisher Scientific) on a rocker. Following the 1-hour block, membranes were then incubated overnight with primary antibodies diluted in blocking solution at 4°C with shaking. Primary antibodies are as follows: dystrophin (1:1000 Invitrogen PA1-21011), exosome CD63 (1:1000, Invitrogen TS63), GAPDH (1:5000 Abcam ab9483), Hsp70 (1:1000, Abcam ab2787), phospho-NF-κB^{Ser536} (1:1000, Cell Signaling Technology 93H1), NF-κB (1:1000, Cell Signaling Technology D14E12), and total OXPHOS (1:1000, Abcam MS604-300). Following the overnight incubation, membranes were washed with TBS-T (3 times 5 minutes) and then probed with the appropriate horseradish peroxidase–conjugated secondary antibody for 2 hours at room temperature. After the secondary incubation, membranes were washed as described and incubated in an enhanced chemiluminescence solution (Thermo Fisher Scientific) and immunoreactivity was visualized using a ChemiDoc (Bio-Rad). Protein abundance was analyzed by densitometry using Image Lab v6.0 software (Bio-Rad).

Histology. The heart and soleus were processed as described (35). Briefly, tissues were embedded in OCT compound and frozen in 2-methylbutane precooled in liquid nitrogen, then stored at –80°C until sectioning. Serial sections of the heart were cut at the mid-papillary level in the transverse plane. Serial sections from the soleus were cut at the mid-belly in the transverse plane. All sections were cut to between 5 and 8 μm using a cryostat (CM3050S, Leica) and adhered to superfrost microscope slides. Cryosections were fixed with 10% neutral buffered formalin for 10 minutes prior to Masson's trichrome (Sigma-Aldrich)

or hematoxylin and eosin staining. Histological slides were imaged using an Aperio AT Turbo slide scanner (Leica) at ×40 magnification. Quantification of fibrosis was determined by the area of blue staining relative to red staining of the entire tissue section using Tissue IA (Leica Biosystems). Myofibers were counted using ImageJ software (NIH).

Immunohistochemistry. Cryosections of the heart and soleus were fixed with acetone (–20°C) for 10 minutes, washed with PBS, and blocked (Protein Block, Dako) for 1 hour at room temperature. Following the 1-hour block, slides were then incubated overnight with primary antibodies diluted in blocking solution at 4°C. Primary antibodies are as follows: CD68 (1:100, Invitrogen MA5-16674), Ki-67 (1:100, Invitrogen MA5-14520), laminin (1:100, Invitrogen MA1-06100), nMHC (1:100, Invitrogen PA5-72846), and α-sarcomeric actinin (1:100, Abcam ab9465). After the overnight incubation, slides were washed with TBS-T (3 times 5 minutes) and incubated with the appropriate Alexa Fluor–conjugated secondary antibody (1:250, Invitrogen) for 2 hours at room temperature. Following the secondary incubation, slides were washed with TBS-T (3 times 10 minutes) and coverslips were mounted with Fluoroshield with DAPI (Sigma-Aldrich) mounting medium. Slides were imaged using confocal fluorescence microscopy (Leica) and quantified using ImageJ software. Pooled data were generated by averaging data from at least 8 fields per heart section and 4 fields per soleus section.

Protein-carbonyl assay. Protein-carbonyl adducts were quantified using a colorimetric kit (Abcam) according to the manufacturer's recommended protocol. Briefly, samples were treated with streptozocin for 15 minutes to neutralize nucleic acids, centrifuged, and the supernatant was transferred to a new tube. 2,4-Dinitrophenylhydrazine was then added and samples were incubated at room temperature for 10 minutes. Following the incubation, trichloroacetic acid was added to the samples that were then vortexed, placed on ice for 5 minutes, and centrifuged. The supernatant was discarded, and the pellet was washed with ice-cold acetone 3 times. After the final wash, guanidine was added to dissolve the pellet. One hundred microliters of each sample was added to a 96-well plate and OD was measured at 375 nm using a spectrophotometer (SpectraMax iD3, Molecular Devices). Carbonylated proteins were quantified with the following equation: nmol carbonyl per mg protein = ([(OD 375 nm)/6.364 × 100] nmol/well)/mg protein

Statistics. Data are represented as mean ± SEM. Statistical significance was determined by independent *t* tests (1-tailed) or 1-way ANOVA using GraphPad Prism v7. Significance was accepted at $P \leq 0.05$. Physiology experiments were conducted as a large cohort a single time. However, when further tissue was required for subsequent biochemical, histological, immunohistochemical, and molecular biology analyses, an appropriate number of mice were similarly treated with vehicle, CDCs, or EXOs.

Study approval. All animal procedures were approved by the Cedars-Sinai Medical Center Institutional Animal Care and Use Committee.

Author contributions

RGR and EM conceived the experiments and wrote the manuscript. RGR, MF, and LS conducted the experiments. RGR analyzed data and performed statistical analyses. AGI, MAA, and MIL helped write the manuscript. EM provided funding to support the study.

Acknowledgments

We gratefully acknowledge expert Illumina sequencing by the UCLA Neuroscience Genomics Core and RNA-seq analysis from Xiangming Ding at TACGenomics. We also thank Lisa Trahan for editorial assistance and support. This work was supported by grants from Coalition Duchenne and NIH grants T32 HL116273 and R01 HL124074 (to EM).

Address Correspondence to: Eduardo Marbán, Director, Smidt Heart Institute, Cedars-Sinai Medical Center, 8700 Beverly Boulevard, 1090 Davis Building, Los Angeles, California 90048, USA. Email: Eduardo.Marban@csmc.edu.

1. Koenig M, et al. The molecular basis for Duchenne versus Becker muscular dystrophy: correlation of severity with type of deletion. *Am J Hum Genet*. 1989;45(4):498–506.
2. Bushby K, et al. Diagnosis and management of Duchenne muscular dystrophy, part 2: implementation of multidisciplinary care. *Lancet Neurol*. 2010;9(2):177–189.
3. Kim S, et al. Associations between timing of corticosteroid treatment initiation and clinical outcomes in Duchenne muscular dystrophy. *Neuromuscul Disord*. 2017;27(8):730–737.

4. Marbán E. A mechanistic roadmap for the clinical application of cardiac cell therapies. *Nat Biomed Eng*. 2018;2(6):353–361.
5. Aminzadeh MA, et al. Reversal of cardiac and skeletal manifestations of Duchenne muscular dystrophy by cardiosphere-derived cells and their exosomes in mdx dystrophic mice and in human Duchenne cardiomyocytes. bioRxiv Web site. https://www.biorxiv.org/content/10.1101/128900v1. Uploaded April 20, 2017. Access March 1, 2019.
6. Ibrahim AG, Cheng K, Marbán E. Exosomes as critical agents of cardiac regeneration triggered by cell therapy. *Stem Cell Reports*. 2014;2(5):606–619.
7. Ibrahim A, Marbán E. Exosomes: fundamental biology and roles in cardiovascular physiology. *Annu Rev Physiol*. 2016;78:67–83.
8. Rogers RG, et al. Intravenous delivery of cardiosphere-derived cells improves striated muscle function and structure in a murine model of Duchenne muscular dystrophy. *FASEB J*. 2017;31(suppl 1):877.10–877.10. https://www.fasebj.org/doi/abs/10.1096/fasebj.31.1_supplement.877.10.
9. Rogers RG, Fournier M, Aminzadeh MA, Gouin K, Sanchez L, and Marbán E. Abstract 16576: Intravenous infusion of cardiosphere-derived cells and their exosomes improve dystrophin-deficient cardiomyopathy in mdx mice. *Circulation*. 2017;136(suppl_1). https://www.ahajournals.org/doi/10.1161/circ.136.suppl_1.16576.
10. Cheng K, et al. Relative roles of CD90 and c-kit to the regenerative efficacy of cardiosphere-derived cells in humans and in a mouse model of myocardial infarction. *J Am Heart Assoc*. 2014;3(5):e001260.
11. Aminzadeh MA, et al. Exosome-mediated benefits of cell therapy in mouse and human models of Duchenne muscular dystrophy. *Stem Cell Reports*. 2018;10(3):942–955.
12. Kim JH, Kwak HB, Thompson LV, Lawler JM. Contribution of oxidative stress to pathology in diaphragm and limb muscles with Duchenne muscular dystrophy. *J Muscle Res Cell Motil*. 2013;34(1):1–13.
13. Malliaras K, et al. Cardiomyocyte proliferation and progenitor cell recruitment underlie therapeutic regeneration after myocardial infarction in the adult mouse heart. *EMBO Mol Med*. 2013;5(2):191–209.
14. Wehling-Henricks M, et al. Macrophages escape Klotho gene silencing in the mdx mouse model of Duchenne muscular dystrophy and promote muscle growth and increase satellite cell numbers through a Klotho-mediated pathway. *Hum Mol Genet*. 2018;27(1):14–29.
15. Zhang J, Ying ZZ, Tang ZL, Long LQ, Li K. MicroRNA-148a promotes myogenic differentiation by targeting the ROCK1 gene. *J Biol Chem*. 2012;287(25):21093–21101.
16. Baumann CW, Rogers RG, Otis JS. Utility of 17-(allylamino)-17-demethoxygeldanamycin treatment for skeletal muscle injury. *Cell Stress Chaperones*. 2016;21(6):1111–1117.
17. Reich H, et al. Repeated transplantation of allogeneic cardiosphere-derived cells boosts therapeutic benefits without immune sensitization in a rat model of myocardial infarction. *J Heart Lung Transplant*. 2016;35(11):1348–1357.
18. Gallet R, et al. Cardiosphere-derived cells reverse heart failure with preserved ejection fraction (HFpEF) in rats by decreasing fibrosis and inflammation. *JACC Basic Transl Sci*. 2016;1(1–2):14–28.
19. Grigorian-Shamagian L, et al. Cardiac and systemic rejuvenation after cardiosphere-derived cell therapy in senescent rats. *Eur Heart J*. 2017;38(39):2957–2967.
20. Middleton RC, Fournier M, Xu X, Marbán E, Lewis MI. Therapeutic benefits of intravenous cardiosphere-derived cell therapy in rats with pulmonary hypertension. *PLoS ONE*. 2017;12(8):e0183557.
21. de Couto G, et al. Exosomal microRNA transfer into macrophages mediates cellular postconditioning. *Circulation*. 2017;136(2):200–214.
22. Yang Y, Li Y, Chen X, Cheng X, Liao Y, Yu X. Exosomal transfer of miR-30a between cardiomyocytes regulates autophagy after hypoxia. *J Mol Med*. 2016;94(6):711–724.
23. Middleton RC, et al. Newt cells secrete extracellular vesicles with therapeutic bioactivity in mammalian cardiomyocytes. *J Extracell Vesicles*. 2018;7(1):1456888.
24. Segawa M, et al. Suppression of macrophage functions impairs skeletal muscle regeneration with severe fibrosis. *Exp Cell Res*. 2008;314(17):3232–3244.
25. Chazaud B, et al. Satellite cells attract monocytes and use macrophages as a support to escape apoptosis and enhance muscle growth. *J Cell Biol*. 2003;163(5):1133–1143.
26. Bencze M, et al. Proinflammatory macrophages enhance the regenerative capacity of human myoblasts by modifying their kinetics of proliferation and differentiation. *Mol Ther*. 2012;20(11):2168–2179.
27. Saclier M, et al. Differentially activated macrophages orchestrate myogenic precursor cell fate during human skeletal muscle regeneration. *Stem Cells*. 2013;31(2):384–396.
28. Porter JD, et al. Persistent over-expression of specific CC class chemokines correlates with macrophage and T-cell recruitment in mdx skeletal muscle. *Neuromuscul Disord*. 2003;13(3):223–235.
29. Rogers RG, de Couto G, Fournier M, Jaghatspanyan E, Sanchez L, Marbán E. Macrophages are required for recovery from physiological muscle stress in the mdx mouse model of muscular dystrophy. *FASEB J*. 2018;32(suppl 1). https://www.fasebj.org/doi/abs/10.1096/fasebj.2018.32.1_supplement.lb438.
30. Estrellas KM, et al. Biological scaffold-mediated delivery of myostatin inhibitor promotes a regenerative immune response in an animal model of Duchenne muscular dystrophy. *J Biol Chem*. 2018;293(40):15594–15605.
31. Taylor M, et al. Cardiac and skeletal muscle effects in the randomized HOPE-Duchenne trial. *Neurology*. 2019;92(8):e866–e878.
32. Marbán E. The secret life of exosomes: What bees can teach us about next-generation therapeutics. *J Am Coll Cardiol*. 2018;71(2):193–200.
33. Baumann CW, Rogers RG, Otis JS, Ingalls CP. Recovery of strength is dependent on mTORC1 signaling after eccentric muscle injury. *Muscle Nerve*. 2016;54(5):914–924.
34. Baumann CW, Rogers RG, Otis JS. Utility of 17-(allylamino)-17-demethoxygeldanamycin treatment for skeletal muscle injury. *Cell Stress Chaperones*. 2016;21(6):1111–1117.
35. Rogers RG, Otis JS. Resveratrol-mediated expression of KLF15 in the ischemic myocardium is associated with an improved cardiac phenotype. *Cardiovasc Drugs Ther*. 2017;31(1):29–38.